Computation of Multiphase Systems with Phase Field Models

V. E. Badalassi [b,*] H. D. Ceniceros [a]

[a] *Department of Mathematics, University of California, Santa Barbara California 93106.*

S. Banerjee [b]

[b] *Department of Chemical Engineering, University of California, Santa Barbara California 93106.*

Abstract

Phase fields models offer a systematic physical approach for investigating complex multiphase systems such as near-critical interfacial behavior, phase separation under shear, and microstructure evolution during solidifications. However, because interfaces are replaced by thin transition regions (diffuse interfaces), phase field simulations require resolution of very thin layers to capture the physics of the problems studied. This demands robust numerical methods that can efficiently achieve high resolution and accuracy, especially in three dimensions. We present here an accurate and efficient numerical method to solve the coupled Cahn-Hilliard/Navier-Stokes system, known as Model H, that constitutes a phase field model for density-matched binary fluids with variable mobility and viscosity. The numerical method is a time-split scheme that combines a novel semi-implicit discretization for the convective Cahn-Hilliard equation with state-of-the-art high resolution CFD schemes employed for direct numerical simulations of turbulence. This new semi-implicit discretization is simple but effective since it removes the stability constraint due to the nonlinearity of the Cahn-Hilliard equation at the same cost as that of an explicit scheme. It is derived from a discretization used for diffusive problems that we further enhance to efficiently solve flow problems with variable mobility and viscosity. For channel geometries, the method uses a spectral discretization in the streamwise and spanwise directions and a combination of spectral and "spectral-like" compact finite difference discretizations in the wall normal direction. The capabilities of the method are demonstrated with several examples including phase separation with, and without, shear in two and three dimensions. The method effectively resolves interfacial layers of as few as three mesh points. The numerical examples show agreement with analytical solutions and scaling laws, where available, and the 3D simulations in the presence of shear reveal rich and complex structures, involving combinations of plates and strings.

Preprint submitted to Elsevier Science *30 July 2002*

Key words: Cahn-Hilliard equation, Navier-Stokes equations, phase separation, Model H, phase separation under shear flow, interface capturing methods.
PACS:

1 Introduction

Phase field based models replace sharp fluid/material interfaces by thin but nonzero thickness transition regions where the interfacial forces are smoothly distributed. The basic idea is to introduce an order parameter or phase field that varies continuously over thin interfacial layers and is mostly uniform in the bulk phases. Perhaps the best-known example of this type of model is the Cahn-Hilliard equation [1,2] used for modeling phase separation in a binary mixture quenched into the unstable region. The relaxation of the order parameter is driven by local minimization of the free energy subject to the phase field conservation and as a result, the interface layers do not deteriorate dynamically.

One of the applications for which phase field models are particularly well-suited is the complex process of phase separation, structure formation and evolution in flow systems, an area of technological impact in soft materials processing. The hydrodynamics can be introduced in several ways. For density-matched binary liquids, which is the case we focus in this work, this is accomplished with the coupling of the convective Cahn-Hilliard equation with a modified momentum equation that includes a phase field-dependent surface force. This is known as the Model H according to the classification of Hohenberg and Halperin [3]. In the case of fluids with different densities a phase field model has been proposed by Lowengrub and Truskinovski [4].

One of the salient points of the phase field description is that the order parameter has a physical meaning and different phenomena can be accounted for by a suitable modification of the free energy. Moreover, complex morphological and topological flow transitions such as coalescence and interface break-up can be captured naturally and in a mass-conservative and energy-dissipative fashion. The main drawback on the other hand is that to properly model relevant physical phenomena the interface layers have to be extremely thin. As a consequence the phase field has large gradients that must be resolved computationally. This is not an easy task. High resolution is required but the

---

[*] Corresponding author.
Email addresses: `badalass@engineering.ucsb.edu` (V. E. Badalassi), `hdc@math.ucsb.edu` (H. D. Ceniceros), `banerjee@engineering.ucsb.edu` (S. Banerjee).

Cahn-Hilliard equation and the phase field-dependent surface force have high order derivative components. Fully implicit treatment of these terms yields expensive schemes and explicit discretizations quickly lead to numerical instability or impose impractical time-stepping constraints.

Here, we propose an efficient and robust numerical method for the coupled Cahn-Hilliard/Navier-Stokes system. The time discretization of the method is a semi-implicit one based on a majorization by constant coefficient terms that are time-step split. The implicit discretization of these constant coefficient terms can be inverted efficiently at optimal cost and relaxes the high order stability constraints. The time splitting allows us to decouple at each time-step the Cahn-Hilliard and the Navier-Stokes solvers. The semi-implicit discretization is combined with state-of-the-art high resolution schemes. For flows confined by walls and with streamwise and spanwise periodicity, we discretize the system in space using a spectral approximation in those directions and a combination of spectral and "spectral-like" (finite order) compact finite difference approximation [5] in the wall normal direction. We demonstrate the efficacy of the method with examples of pure phase separation and binary shear flow in two and three dimensions. Little work has been done for the solution of the coupled Cahn-Hilliard/Navier-Stokes system [6–9] and our three-dimensional simulations for separation under shear flow are, to our knowledge, one of the first ever reported. The overall method proposed here is accurate and robust allowing interface thickness of as few as three mesh points and, as the numerical experiments show, its efficiency makes possible high-resolution 3D simulations in even modest personal computers. The numerical examples show agreement with analytical solutions and scaling laws where available and the 3D simulations in the presence of shear flow reveal rich and complex structures characterized by combinations of plates and strings.

The rest of the paper is organized as follows: the next section gives a brief introduction to the model coupling the phase field and the Navier-Stokes equations. Section 3 discusses our proposed numerical procedure, and in Section 4 the method is validated through numerical examples. This is followed by some concluding remarks.

2 The Governing Equations

2.1 The Phase Field Method

Phase field methods are a particular class of diffused-interface models that have been very successful in the study of critical phenomena but have not been used much for fluid interfaces. In a phase field method, it is assumed that the state of the system at any given time can be described by an order parameter ϕ which is a function of the position vector. For example, in the case of an isothermal binary fluid ϕ identifies the relative concentration of the two components. A free energy can be defined for times when the system is not in equilibrium [10], and this free energy can be written as a functional of ϕ:

$$F[\phi] = \int_{\Omega} \left\{ f(\phi(\mathbf{x})) + \frac{1}{2} k |\nabla \phi(\mathbf{x})|^2 \right\} d\mathbf{x}, \tag{1}$$

where Ω is the region of space occupied by the system. The term $\frac{1}{2}k|\nabla\phi(\mathbf{x})|^2$ accounts for the surface energy, with k a positive constant, and $f(\phi(\mathbf{x}))$ is the bulk energy density which has two minima corresponding to the two stable phases of the fluid.

The chemical potential μ is defined as

$$\mu(\phi) = \frac{\delta F[\phi]}{\delta \phi(\mathbf{x})} = f'(\phi(\mathbf{x})) - k\nabla^2\phi(\mathbf{x}). \tag{2}$$

The equilibrium interface profile can be found by minimizing the functional $F[\phi]$ with the respect to variations of the function ϕ, i.e. solving $\mu(\phi) = 0$. Cahn and Hilliard [1,2] generalized the problem to time-dependent situations by approximating interfacial diffusion fluxes as being proportional to chemical potential gradients, enforcing conservation of the field. The convective Cahn-Hilliard equation can be written as

$$\frac{\partial \phi}{\partial t} + \mathbf{u} \cdot \nabla \phi = \nabla \cdot (M(\phi)\nabla\mu), \tag{3}$$

where $\mathbf{u}$ is the velocity field and $M(\phi) > 0$ is the mobility or Onsager coefficient. Equation (3) models the creation, evolution, and dissolution of diffusively controlled phase-field interfaces [11] (for a review of the Cahn-Hilliard model see for example [12]). At the wall, we adopt the following no-flux boundary conditions:

$$\mathbf{n} \cdot \nabla\phi = 0 \quad \text{and} \quad \mathbf{n} \cdot M\nabla\mu = 0, \tag{4}$$

where $\mathbf{n}$ is the unit vector normal to the domain boundary.

2.2 The Equations of Fluid Motion

This work focuses on density-matched binary mixtures with variable viscosity and mobility. The fluid dynamics are described by the Navier-Stokes equations with a phase field-dependent surface force [13]:

$$\rho\left(\frac{\partial \mathbf{u}}{\partial t} + \mathbf{u}\cdot\nabla\mathbf{u}\right) = -\nabla p + \nabla\cdot\eta(\nabla\mathbf{u} + \nabla\mathbf{u}^T) + \mu\nabla\phi, \tag{5}$$

$$\nabla\cdot\mathbf{u} = 0, \tag{6}$$

where $\mathbf{u}$ is the velocity field, p is the pressure that enforces the incompressibility constraint (6), and η is the viscosity. The superscript T stands for the transpose operator. At a wall the no-slip boundary condition is imposed for the velocity field, i.e., $\mathbf{u} = 0$ at a fixed domain boundary.

The coupled Cahn-Hilliard/Navier-Stokes system (3) – (6) is referred to as "Model H" according to the nomenclature of Hohenberg and Halperin [3].

2.3 Interface Properties

For the binary fluid we use the following double well potential

$$f(\phi) = \frac{\alpha}{4}\left(\phi - \sqrt{\frac{\beta}{\alpha}}\right)^2\left(\phi + \sqrt{\frac{\beta}{\alpha}}\right)^2, \tag{7}$$

where α and β are two positive constants. The equilibrium profile is given by the solutions of the equation

$$\mu(\phi) = \frac{\delta F[\phi]}{\delta\phi} = \alpha\phi^3 - \beta\phi - k\nabla^2\phi = 0. \tag{8}$$

This leads to two stable uniform solutions $\phi_\pm = \pm\sqrt{\frac{\beta}{\alpha}}$ representing the coexisting bulk phases, and a one-dimensional (say along the z-direction) non-uniform solution

$$\phi_0(z) = \phi_+ \tanh\left(\frac{z}{\sqrt{2}\xi}\right) \tag{9}$$

that satisfies the boundary conditions $\phi_0(z \to \pm\infty) = \pm\phi$ (see [14,6]). This solution was first found by Van der Waals [15] to describe the equilibrium profile for a plane interface normal to the z direction, of thickness proportional to $\xi = \sqrt{k/\beta}$, and that separates the two bulk phases.

We define the interface thickness to be the distance from $0.9\phi_-$ to $0.9\phi_+$ so that the equilibrium interface thickness is $2\sqrt{2}\xi \tanh^{-1}(0.9) = 4.164\xi$. This width contains 98.5% of the surface tension stress [7].

In equilibrium the surface tension σ of an interface is equal to the integral of the free energy density along the interface. For a plane interface σ is given by [14]

$$\sigma = k \int_{-\infty}^{+\infty} \left(\frac{d\phi_0}{dz}\right)^2 dz = \frac{\sqrt{2}}{3} \frac{k^{1/2}\beta^{3/2}}{\alpha}. \tag{10}$$

It is evident from (9) and (10) that we can control the surface tension and interface width through the parameters k, α, and β.

2.4 Nondimensionalization

We nondimensionalize the governing equations with the variables

$$\mathbf{u}' = \frac{\mathbf{u}}{U_c}, \quad t' = \frac{t}{T_c}, \quad \mathbf{x}' = \frac{\mathbf{x}}{L_c}, \quad p' = \frac{pL_c}{\eta_c U_c}. \tag{11}$$

Following Chella and Viñals [6] we choose as characteristic length L_c the mean field thickness ξ of the interface, i.e $L_c = \xi$. The characteristic velocity U_c depends on the problem; for example, it could be the imposed velocity in shear flow. The characteristic time T_c is the time required for the fluid to be convected a distance of the order of the interface thickness (in the absence of capillarity), $T_c = \xi/U_c$. The order parameter ϕ is scaled with its mean-field equilibrium value $\phi_+ = \sqrt{\beta/\alpha}$. Dropping the primes, equations (3)-(6) become

$$\frac{\partial \phi}{\partial t} + \mathbf{u} \cdot \nabla\phi = \frac{1}{Pe} \nabla \cdot \lambda \nabla \mu, \tag{12}$$

$$Re\left(\frac{\partial \mathbf{u}}{\partial t} + \mathbf{u} \cdot \nabla \mathbf{u}\right) = -\nabla p + \nabla \cdot \theta(\nabla \mathbf{u} + \nabla \mathbf{u}^T) + \frac{1}{Ca}\mu \nabla \phi, \tag{13}$$

$$\nabla \cdot \mathbf{u} = 0, \tag{14}$$

where $\theta = \eta/\eta_c$ and $\lambda = M/M_c$ are the normalized viscosity and the mobility respectively and $\mu = \phi^3 - \phi - \nabla^2\phi$ is the dimensionless chemical potential.

The dimensionless groups used above are the Reynolds number, the Péclet number, and the capillary number given by

$$Re = \frac{\rho U_c \xi}{\eta}, \quad Pe = \frac{U_c \xi}{M_c \beta}, \quad Ca = \frac{\alpha \eta U_c}{\beta^2 \xi} = \frac{2\eta U_c}{3\sigma}, \tag{15}$$

respectively. Physically, the Péclet number Pe is the ratio between the diffusive time scale $\xi^2/(M_c\beta)$ and the convective time scale ξ/U_c. The Reynolds number Re is the ratio between inertial and viscous forces and the capillary number Ca provides a measure of the relative magnitude of viscous and capillary (or interfacial tension) forces at the interface. Note that with this nondimensionalization the length of the fluid domain is interpreted in units of interface thickness ξ.

We consider the viscosity η as a linear function of the order parameter ϕ. That is, if $\eta_- \leq \eta \leq \eta_+$ and $\eta_c = \eta_-$ we get

$$\theta = \frac{\theta_{\max} - 1}{2}\phi + \frac{\theta_{\max} + 1}{2}, \tag{16}$$

where $\theta_{\max} = \frac{\eta_+}{\eta_-}$ is the viscosity ratio. In this way η get automatically diffused across the interface with a profile similar to the tanh function.

For the mobility M we follow [16] and we consider a profile as $M = M_c\,(1 - \gamma\phi^2)$ so that we have

$$\lambda = \left(1 - \gamma\phi^2\right). \tag{17}$$

where $0 \leq \gamma \leq 1$. If $\gamma \longrightarrow 0$ we have phase separation dynamics controlled by bulk diffusion, if $\gamma \longrightarrow 1$ we have dynamics controlled by interface diffusion.

3 The Numerical Method

The numerical method we propose is based on a semi-implicit time discretization combined with a time-split strategy. This discretization effectively decouples Cahn-Hilliard and Navier-Stokes solvers and yields an efficient and robust modular scheme.

The outline of the method is as follows. Given ϕ^n and $\mathbf{u}^n$ the objective is to solve for ϕ^{n+1} and $\mathbf{u}^{n+1}$ with the steps:

(1) Solve the Cahn-Hilliard equation with a semi-implicit method and spectral spatial discretization to obtain ϕ^{n+1}.

(2) Using ϕ^{n+1} compute the surface force and solve the phase-field modified Navier-Stokes equations with a standard projection method to obtain $\mathbf{u}^{n+1}$. The spatial discretization is spectral in the streamwise and spanwise directions and a combination of spectral and "spectral-like" compact finite difference in the wall normal direction [5,17,18].

These two steps consist of first order semi-implicit Euler time advancements. To achieve a higher accuracy we embed them in a third order Runge-Kutta method as described below. We provide next the details of both the temporal and the spatial discretization.

3.1 Time Discretization

Our semi-implicit strategy uses a simple idea that works quite well for diffusion-dominated equations, for example the variable (even nonlinear) coefficient diffusion equation $u_t = \nabla \cdot (\chi \nabla u)$, $\chi > 0$ [19,20]. This discretization consists in replacing the variable coefficient term with a constant coefficient one in the first order implicit discretization:

$$\frac{u^{n+1} - u^n}{\Delta t} = a\nabla^2 u^{n+1} + \nabla \cdot (\chi^n \nabla u^n) - a\nabla^2 u^n, \tag{18}$$

where Δt is the time step and a is constant in space (but could be time-dependent). With energy estimates one can show that this discretization is unconditionally stable if $a \geq \frac{1}{2} \max \chi$ and since the truncation error is dissipative and proportional to a, we consider $a = \frac{1}{2} \max \chi$ as an optimal value. Discretizations of this type are of common use in spectral methods [20] as the constant coefficient implicit terms becomes diagonal in Fourier space and thus can be inverted efficiently. However, as noted in [21], these discretizations are less successful for dispersion-dominated problems.

We can apply this type of discretization directly to deal with variable mobility. However, the application of the same idea to the treatment of the nonlinear term due to the chemical potential is not straightforward. To achieve this, we note that $\nabla^2 f'(\phi) = \nabla \cdot (f'' \nabla \phi)$ where $f'(\phi) = \phi^3 - \phi$ and $f''(\phi) = 3\phi^2 - 1$. Letting $\tau = \frac{1}{2} \max (f'(\phi)) = \frac{1}{2} f''(\pm 1) = 1$ and defining $\lambda_{\max} = \max \lambda$ as the maximum of the normalized mobility (the mobility ratio if $M_c = M_-$) we discretize (12) in time with the semi-implicit Euler step:

$$\frac{\phi^{n+1} - \phi^n}{\Delta t} = \frac{1}{Pe} \left[-\frac{\lambda_{\max}}{2} \nabla^4 \phi^{n+1} + \frac{\lambda_{\max}}{2} \tau \nabla^2 \phi^{n+1} + \nabla \cdot \lambda^n \nabla f'(\phi^n) \right.$$

$$-\frac{\lambda_{\max}}{2}\tau\nabla^2\phi^n - \nabla\cdot\lambda^n\nabla(\nabla^2\phi^n) + \frac{\lambda_{\max}}{2}\nabla^4\phi^n\Bigg]$$
$$- \mathbf{u}^n\cdot\nabla\phi^n. \tag{19}$$

At each time-step (19) can be solved for ϕ^{n+1} efficiently at essentially the cost of an explicit method. In the absence of convection, this new discretization appears in our numerical experiments to be *unconditionally stable*. Eyre [22] considers a discretization of this type for the one-dimensional Cahn-Hilliard equation with constant mobility while Zhu, Chen, Shen, and Tikare [23] use it for the mobility term but not for the nonlinear one, resulting in a conditionally stable method.

For the Navier-Stokes equations (13)-(14) we use a standard Chorin projection method [24] combined with the above semi-implicit discretization applied to the variable viscosity term:

Step 1:

$$\frac{\mathbf{u}^* - \mathbf{u}^n}{\Delta t} + \mathbf{u}^n\cdot\nabla\mathbf{u}^n = \frac{1}{Re}\Bigg[\frac{\theta_{\max}}{2}\nabla^2\mathbf{u}^* + \nabla\cdot\theta^{n+1}(\nabla\mathbf{u}^n + (\nabla\mathbf{u}^n)^T)$$
$$- \frac{\theta_{\max}}{2}\nabla^2\mathbf{u}^n + \frac{1}{Ca}\mu(\phi^{n+1})\nabla\phi^{n+1}\Bigg] \tag{20}$$

Step 2:

$$\nabla^2 p^{n+1} = \frac{Re}{\Delta t}\nabla\cdot\mathbf{u}^*, \tag{21}$$

Step 3:

$$\mathbf{u}^{n+1} = \mathbf{u}^* - \frac{\Delta t}{Re}\nabla p^{n+1}. \tag{22}$$

Evaluating the normal component of (22) at the boundary we get the standard numerical boundary condition for the pressure:

$$\left.\frac{\partial p^{n+1}}{\partial n}\right|_\Gamma = -\frac{Re}{\Delta t}(\mathbf{u}_\Gamma^{n+1} - \mathbf{u}_\Gamma^*)\cdot\mathbf{n}, \tag{23}$$

where the subscript Γ denotes evaluation at the domain boundary. Here we opt for the commonly used choice $\mathbf{u}_\Gamma^* = \mathbf{u}_\Gamma^{n+1}$. Thus (21) is solved with the homogeneous Neumann condition

$$\left.\frac{\partial p^{n+1}}{\partial n}\right|_{\Gamma} = 0. \tag{24}$$

which guarantees the convergence to the exact velocity [25], albeit at the cost of introducing a numerical boundary layer for the auxiliary variables p and $\mathbf{u}^*$, but not for $\mathbf{u}^{n+1}$ [26–28].

Following Kang, Fedkiw, and Liu [29] we embed the Euler step into a third order Runge-Kutta method. To simplify notation, we use E to define an Euler update and $\mathbf{V} = (\phi, \mathbf{u})$, so symbolically

$$\mathbf{V}^{n+1} = E(\mathbf{V}^n). \tag{25}$$

A third order Total Variation Diminishing (TVD) Runge-Kutta is obtained using convex combinations of the Euler step [30]:

$$\mathbf{V}^{n+1} = \frac{1}{3}\mathbf{V}^n + \frac{2}{3}E\left(\frac{3}{4}\mathbf{V}^n + \frac{1}{4}E(E(\mathbf{V}^n))\right). \tag{26}$$

Note that the third order Runge-Kutta allows a very easy implementation of adaptive time stepping. Further, it has a larger stability region than that of the second order one and its stability region also includes a part of the imaginary axis.

3.2 Spatial Discretization

We employ high-resolution spatial discretizations to be able to accurately resolve thin interfaces. The Cahn-Hilliard equation is discretized in space (pseudo) spectrally (via FFT for periodic boundary conditions or Cosine transform for the no-flux conditions). For the Navier-Stokes equations we use spectral derivatives in the streamwise and spanwise (periodic) directions and a “spectral-like” finite difference compact scheme [5] for the wall normal derivatives of the velocity. The cosine transform is used for the Poisson equation in order to satisfy automatically (24) and have a spectral resolution. Spectral-like accuracy is critical as interface layers of only a few mesh points need to be resolved and numerical diffusion has to be limited to avoid unphysical coalescence.

The first step of the projection method (20) deserves further comments; we rewrite it as

$$\frac{2Re}{\theta_{\max}}\frac{\mathbf{u}^*}{\Delta t}-\nabla^2\mathbf{u}^*=\frac{2Re}{\theta_{\max}}\left(\frac{\mathbf{u}^n}{\Delta t}-\mathbf{u}^n\cdot\nabla\mathbf{u}^n\right)+\frac{2}{\theta_{\max}Ca}\mu(\phi^{n+1})\nabla\phi^{n+1}$$
$$+\frac{2}{\theta_{\max}}\left[\nabla\cdot\theta^{n+1}(\nabla\mathbf{u}^n+(\nabla\mathbf{u}^n)^T)-\frac{\theta_{\max}}{2}\nabla^2\mathbf{u}^n\right].\quad(27)$$

Since we have periodic boundary conditions in the horizontal direction we can Fourier transform to obtain (dropping the asterisk)

$$\left(\frac{2Re}{\theta_{\max}\Delta t}+k_x^2+k_y^2\right)\hat{\mathbf{u}}-\hat{\mathbf{u}}''=\widehat{\Omega}\left(k_x,k_y,z\right),\quad(28)$$

where the prime denotes derivative with respect to z, $\Omega(x,y,z)$ is the left-hand side of (27) and the caret stands for the 2D Fourier transform in the streamwise direction. Thus (i is the z-index of the grid)

$$\hat{\mathbf{u}}_i''=k^2\hat{\mathbf{u}}_i-\widehat{\Omega}_i,\quad(29)$$

where $k^2=\frac{Re}{\theta_{\max}\Delta t}+k_x^2+k_y^2$. A “spectral-like” finite difference compact scheme discretization of (29) (see the Appendix for details) yields the eptadiagonal system

$$D\hat{u}_{i-3}+C\hat{u}_{i-2}+B\hat{u}_{i-1}+A\hat{u}_i+B\hat{u}_{i+1}+C\hat{u}_{i+2}+D\hat{u}_{i+3}=$$
$$\beta\widehat{\Omega}_{i-2}+\alpha\widehat{\Omega}_{i-1}+\widehat{\Omega}_i+\alpha\widehat{\Omega}_{i+1}+\beta\widehat{\Omega}_{i+2},\quad(30)$$

where $A=k^2+\left(b/2+2a+2c/9\right)/\left(\Delta z\right)^2$, $B=\alpha k^2-a/\left(\Delta z\right)^2$, $C=\beta k^2-b/\left(2\Delta z\right)^2$, $D=-c/\left(3\Delta z\right)^2$. The parameters a, b, c, α and β (given in the Appendix) are chosen to achieve “spectral-like” resolution [5]. The narrow-banded system (30) is solved with a generalized Thomas algorithm.

Note that compact finite difference approximations are used only for the wall normal derivatives of the velocity in (20)-(21). We compute the other derivatives spectrally in the x and y directions with the fast Fourier transform (FFT) and in the z direction using discrete sine (DST) and cosine (DCT) transforms (see Appendix).

4 Numerical Experiments and Validation

We present three types of numerical experiments to validate the proposed method and test its capabilities . The experiments are simulations of pure spinodal decomposition, drop deformation and phase separation under shear flow. A resolution study is also performed to check the accuracy and the stability of the method. This is briefly described next.

4.1 Accuracy and Stability

To test the accuracy of the time discretization we perform a sequence of simulations for a single flat interface keeping the spatial resolution fixed and halving subsequently the time step. Denoting by $\mathbf{V}(\Delta t) = (\phi, \mathbf{u})$ the approximation obtained using a step-size Δt, we compute the error ratios

$$R(\Delta t) = \frac{|\mathbf{V}(\Delta t) - \mathbf{V}(\Delta t/2)|}{|\mathbf{V}(\Delta t/2) - \mathbf{V}(\Delta t/4)|}, \tag{31}$$

and find that they are close to the value eight which corresponds to third order accuracy in time.

A rigorous stability analysis for the overall scheme is quite difficult. Nevertheless one can obtain valuable information about the stability and robustness of the scheme through numerical tests. In particular, through numerical experiments we find that the semi-implicit discretization (19) for the Cahn-Hilliard equation appears to be *unconditionally stable* when $\mathbf{u} \equiv \mathbf{0}$, *regardless of the interface thickness*. Moreover, the unconditional stability seems to hold for $a \geq f''(\pm 1)/2 = 1$ just as for the corresponding discretization of the variable diffusion equation $u_t = \nabla \cdot (\chi \nabla u)$. Thus, for a given nonzero $\mathbf{u}$, the scheme for the convective Cahn-Hilliard equation has only a CFL stability condition:

$$\Delta t_{cfl} \leq \left(\frac{|u|_{\max}}{\Delta x} + \frac{|v|_{\max}}{\Delta y} + \frac{|w|_{\max}}{\Delta z} \right)^{-1}, \tag{32}$$

where (u, v, w) are the components of the velocity field.

When coupled with the time discretization of the modified Navier-Stokes equations (20)- (22), in addition to the natural CFL condition, we have to consider time step restrictions due to surface tension and viscosity. For the surface tension we observe a mild stability constraint of the form

$$\Delta t_s \leq C_1 \sqrt{ReCa} \; \left(\min\{\Delta x, \Delta y, \Delta z\} \right)^{3/2}, \tag{33}$$

where C_1 is a constant. $C_1 = 10$, works well for all our numerical examples. Note that spatial mesh sizes are nondimensional so that $\min(\Delta x, \Delta y, \Delta z) = O(1)$. The same type of condition is found for capturing ("color") methods (with the appropriate nondimensionalization) such as the Level Set Method [31] and the continuum surface force method (CSF) [32] that rely both on less stiff evolution equations for the "color" function.

We now derive the stability constraint associated with the variable viscosity term. Using the incompressibility condition, the Navier-Stokes equations (13) in indicial notation (repeated index summation implied) become

$$\left(\frac{\partial u_i}{\partial t} + u_k \frac{\partial u_i}{\partial x_k}\right) = -\frac{1}{Re}\frac{\partial p}{\partial x_i} + \frac{1}{Re}\left\{\frac{\partial}{\partial x_k}\left(\theta \frac{\partial u_i}{\partial x_k}\right) + \frac{\partial \theta}{\partial x_k}\frac{\partial u_k}{\partial x_i}\right\} + \frac{1}{CaRe}\mu \frac{\partial \phi}{\partial x_i}. \tag{34}$$

The semi-implicit discretization removes the severe stability constraint due to the term $\frac{\partial}{\partial x_k}\left(\theta \frac{\partial u_i}{\partial x_k}\right)$ but has limited effect on the term $\frac{\partial \theta}{\partial x_k}\frac{\partial u_k}{\partial x_i}$. This term gives rise to a CFL-like stability constraint that can be determined by estimating $\max|\nabla\theta|$. In the limit of gently curved interfaces, and when the motion of the interface is slow compared with the local relaxation times of ϕ, we can approximate ϕ by the one-dimensional stationary solution ϕ_0 in (9) along the direction normal to the interface, i.e. $\nabla\phi \simeq \nabla\phi_0$. From (9) and (16) we have that $\nabla\theta \propto (\theta_{\max} - 1)\,\mathrm{sech}^2 x$, then $\max|\nabla\theta| \propto (\theta_{\max} - 1)$. Thus, the variable viscosity time-step constraint has the form

$$\Delta t_{vr} \leq C_2 \frac{Re}{\theta_{\max} - 1}\left(\min\{\Delta x, \Delta y, \Delta z\}\right), \tag{35}$$

where C_2 is a constant. For $\theta_{\max} = 1$ the discretization is unconditionally stable since it reduces to an implicitly treated constant viscosity case. For $\theta_{\max} > 1$ we could use successfully $C_2 = 10$ for all our simulations. Note that if we were treating the viscous term purely explicitly we would have the more restrictive constraint $\Delta t \leq \frac{Re}{\theta_{\max}}[(\Delta x)^{-2} + (\Delta y)^{-2} + (\Delta z)^{-2}]^{-1}$.

We can now express our adaptive time stepping strategy as

$$\Delta t^{n+1} = \min\left(\Delta t_{cfl}, \Delta t_s, \Delta t_{vr}\right). \tag{36}$$

The discretization (19) effectively removes the high order stability constraints associated with the Cahn-Hilliard equation and makes the phase field-based method computationally competitive and robust. To relax more the viscous stability constraint in the case of very small Re one can use a predictor-corrector iteration strategy. Increasing the "majorizing" constant diffusion term in (20) also relaxes the constraint by allowing a larger constant C_2, albeit at the cost of increasing the truncation error. For example if $\theta_{\max}$ is used instead of $\frac{1}{2}\theta_{\max}$ we find that one can use $C_2 = 180$ giving a significant saving in time stepping.

4.2 Drop Deformation in a Shear Flow

We consider an initially 2D spherical drop in a shear flow. This is a classical problem that was solved analytically for sharp interfaces and small deformations in the creeping flow approximation for unbounded domain by Taylor [33] and in the presence of two walls by Shapira and Haber [34]. The drop will undergo a deformation that depends on the capillary number and the viscosity ratio. We use this problem to demonstrate the convergence of the numerical results under grid refinement. At the same time, we validate the calculation of surface tension and density ratio in a qualitative fashion (we have very small but finite Reynolds number, interface thickness, and drop deformation). We employ an interface thickness of only three mesh points, similar to the thickness used in other capturing methods.

As initial condition we start with a circular drop in the center of the domain with a "tanh" profile of the interface and we solve the Cahn-Hilliard equation without convection to reach a steady state that leads to a completely saturated mixture. Then we impose a shear flow with the top and bottom lid moving in opposite directions and with the dimensionless velocity equal to plus or minus one, respectively. We consider three capillary numbers $Ca = 0.6$, 0.9, and 1.2. The fluids have the same viscosity and $Re = 0.1$, $Pe = 10$. We employ two resolutions 128×128 and 256×256, and domain sizes of $L = 178$ and $L = 355$, respectively. This combination of parameters determines an interface thickness of three mesh points. In Figure 1 we plot the final equilibrium stage. It is evident the convergence of the results under grid refinement. The drop shape is ellipsoidal with the major axis converging to an angle of 45^o as Ca decreases, just as the predicted by the analytic results [33,34]. Moreover, the contours -0.9 and 0.9 describing the interface are well behaved since they stay perfectly parallel throughout the computation. Increasing the capillary number results in an increased deformation and the angle diminishes in the direction of the major axis to the undisturbed (horizontal) streamlines. This result matches the numerical result of Rallison [35] for deformations where the analytical solution is not available.

We now consider the case of variable viscosity. Shown in Figure 2 are the results for $Pe = 10$, $Re = 0.1$, $Ca = 0.8$,. Three viscosity ratios are considered: $\theta_{\max} =$ 2, 5, and 10. We plot the contour of $\phi = 0$ only. The deformation increases as predicted in [33,34] without any appreciable change in the orientation.

We begin the numerical experiments with an example of pure spinodal phase separation of a binary mixture. An initially homogeneous disordered phase separates into order structures when quenched into a metastable region. The Cahn-Hilliard equation (without convection) models this process. For pure phase separation it is convenient to nondimensionalize (3), with $\mathbf{u} = 0$, using variables (11) with L_c as the domain size and $T_c = M_c\beta$. Dropping the primes, equation (3) becomes

$$\frac{\partial\phi}{\partial t} = \nabla \cdot \left(1 - \gamma\phi^2\right) \nabla(f'(\phi) - C^2\nabla^2\phi), \tag{37}$$

where $C = \xi/L_c$ is the Cahn number and $f'(\phi) = \phi^3 - \phi$. The Cahn number represents the ratio between the interface thickness and the domain size. Characteristic properties of (37) are the conservation of the order parameter [12]

$$\frac{d}{dt}\int_\Omega \phi(t, \mathbf{x})d\mathbf{x} = 0, \tag{38}$$

and a monotonic decrease in the total energy

$$\frac{d}{dt}F[\phi] = \int_\Omega \left\{ f(\phi) + \frac{C^2}{2}|\nabla\phi|^2 \right\} d\mathbf{x} \leq 0. \tag{39}$$

We take as initial condition a random perturbation of a uniform mixture as follows

$$\phi(0, \mathbf{x}) = \phi_m + Cr(\mathbf{x}), \tag{40}$$

where the random $r(\mathbf{x})$ is in $[-1, 1]$ and has zero mean. ϕ_m is the constant concentration of the uniform mixture. The domain is the unit square.

In our first example we consider periodic boundary conditions, constant mobility ($\gamma = 0$) and $\phi_m = 0$ which corresponds to the well known case of spinodal phase separation controlled by bulk diffusion. We take $C = 7.03 \times 10^{-4}$ and using a spatial mesh of 1024×1024 points we have interfacial thickness of three points. According to linear analysis (see e.g. [36]) the fastest growth rate is $1/(4C^2)$. The solution quickly develops two spatial length scales, one associated with the wavelength λ of the fastest growing mode and the other, the shortest one, with the transitions between phases. For $\phi_m = 0$, $\lambda = 2\pi\sqrt{2}C$, while the phase transition layers are approximately of size C and thus a mesh size of $O(C)$ is needed. After the fast initial stage the dynamics are very slow and it takes a long time to reach a quasi-stationary state. With the third order semi-implicit scheme we can compute stably the solution and resolve both the fast initial dynamics and the slow long-time behavior varying Δt to adjust to the dynamics while at the same time affording the required high spatial resolution.

Figure 3 shows snapshots of the solution plotted as flooded contours. The red color corresponds to $\phi = 1$ and the blue to $\phi = -1$. The initially homogeneous mixture undergoes a fast separation followed a slow coarsening where the typical spinodal structures can be observed. Due to the very small Cahn number and the high resolution the interfaces separating the structures appear fairly sharp. We start the computation with $\Delta t = 4.95 \times 10^{-7}$ to resolve the solution fastest growth, but we only compute with this time-step up to $t = C = 7.03 \times 10^{-4}$; for the longer time computation we use $\Delta t = 0.0002$. This time-step selection is purely based on accuracy as the method appears to be unconditionally stable and any choice of Δt produces a stable computation.

As shown in [37] a two-phase morphology undergoing coarsening can be characterized by the time-dependent structure function

$$S(\mathbf{k}, t) = \frac{1}{N} \left\langle \sum_{\mathbf{r}} \sum_{\mathbf{r}'} e^{-i\mathbf{k}\cdot\mathbf{r}} \left[\phi(\mathbf{r} + \mathbf{r}', t)\, \phi(\mathbf{r}', t) - \langle \phi \rangle^2 \right] \right\rangle, \tag{41}$$

where both sums run over the lattice, N is the total number of points in the lattice, and <> stands for average over all lattice points. The normalized structure function $s(k, t)$ is given by

$$s(k, t) = \frac{S(k, t)}{N \left[\langle \phi^2(\mathbf{r}) \rangle - \langle \phi^2 \rangle \right]} \tag{42}$$

and we can characterize the typical length scale $R(t)$ with the first moment of $s(k, t)$ [23],

$$k_1(t) = \frac{\sum k s(k, t)}{\sum s(k, t)}. \tag{43}$$

In Figure 4 we plot the normalized and circularly averaged structure function at five different time steps. The lines are spline fits to the simulation data. As time increases, the maximum value of the structure function increases and shifts to lower k, indicating an increase in the real-space average length scale. This is consistent with the results reported in [23]. In Figure 5 we plot the cubic of the average domain size versus time. The straight line behavior confirms the expected cubic growth law [23].

We now consider a case of variable mobility by setting $\gamma = 0.9$. Figure 6 shows the morphological evolution of the mixture for $\phi_m = 0$ and Cahn number $C = 0.001$ using a 1024×1024 resolution. This is the case of interface diffusion controlled coarsening that is characterized by a much slower dynamics but with similar morphological patterns. These results are analogous to the ones reported in [23]. But here, with the unconditionally stable scheme, we are able use a large time step ($\Delta t = 0.01$) to follow the very slow coarsening dynamics. Moreover, we can resolve a thinner interface of only three mesh points and with a third order time integration.

We turn now to two 3D simulations of pure phase separation with constant mobility ($\gamma = 0$) and no-flux boundary conditions, i.e. $\mathbf{n} \cdot \nabla\phi = 0$ and $\mathbf{n} \cdot \nabla(f'(\phi) - C^2\nabla^2\phi) = 0$ (Figure 7 and 8). We take first $\phi_m = 0$ and $C = 0.01$ and we render the iso-surface of separation of the two fluids at $\phi = 0$. Figure 7 depicts representative snapshots of iso-surface. Notice the complexity of the patterns that cannot be extrapolated from the 2D counterpart. The simulation begins with $\Delta t = 2.5 \times 10^{-4}$ up to $t = C = 0.01$ and for longer times $\Delta t = 0.01$ is used. Figure 8 presents very different separation morphology. For this simulation we take $\phi_m = -0.5$ and we render the initial stages using $\Delta t = 2.5 \times 10^{-4}$. The initial uniform mixture evolves into a system consisting of a large array of round particles at $t = 0.01$. The coarsening takes place and the spherical drops grow until they coalesce.

Figure 9 shows the time-behavior of the phase field mean and the energy for a spinodal decomposition with a resolution of $128 \times 128 \times 128$. We find that the mean is preserved within 3 to 4 digits and the energy decreases monotonically (and smoothly) throughout the entire computation as required by (39).

4.4 2D & 3D Spinodal Decomposition and Pattern Formation in a Channel under Shear

We consider the spinodal decomposition of a density-matched binary fluid mixture in a channel under shear. As we will see the linear shear plays a crucial role in the morphology and evolution of the patterns. The initial conditions are a random perturbation around the uniform concentration $\phi = 0$. Figure 10(a) and Figure 10(b) show 2D results at two shear rates with the top lid and bottom lid moving horizontally in opposite directions. The shear rate is defined as $sr = U_c/h$ where h is the distance between the two plates.

Since we impose a fixed geometry, $sr \propto U_c$. Thus, to change the shear rate we need to change Pe, Re and Ca accordingly as they all contain U_c. The flow in Figure 10(b) has five time the shear rate as that in Figure 10(a). We notice that after a transient stage characterized by the formation of patterns in the mixture under the influence of the Cahn-Hilliard term (spinodal decomposition), the domains get elongated into long layers against their intrinsic surface tension instabilities. Moreover, the patterns formed in the early stage are quite different when the shear velocity increases, and the number of layers in the late stage increases when the shear rate is higher. This behavior is in accordance with experiments reported in [38] and simulations in [9].

In Figure 11 we consider a 3D simulation in the presence of shear. Here the structures are much more complex with plates and strings forming. Stringlike structures have been observed in polymer blends which are thermodynamically near a phase transition point [39,40] and in immiscible viscoelastic systems in complex flow fields [41] and in dispersed droplets [41]. There is great current interest in micro and nano length scale technologies in which polymer blends could play an important role. For example, if we create strings with a conductive material in an insulating matrix with good mechanical properties, then one could produce wires. In other ways [41] it might be possible to manufacture ultrathin materials of high one-dimensional strength or scaffolds. A detailed study of the string process formation with our numerical procedure is under current investigation and it will be reported elsewhere. The methodology presented here appears quite promising for the design and analysis of multiphase and complex fluid formulations.

5 Concluding Remarks

An accurate and efficient numerical method for computing phase ordering kinetics coupled with fluid dynamics was presented. The numerical method is based on semi-implicit time discretizations and high-resolution spatial discretizations of the coupled Cahn-Hilliard/Navier-Stokes system. The numerical method is robust and has a cost comparable to an explicit method. Some of the capabilities of the method were illustrated with numerical examples in two and three dimensions, including the technologically important problem of phase separation under shear flow. In particular, the 3D simulations in the presence of shear flow reveal rich and complex structures characterized by a combined formation of plates and strings. The method can be extended to general geometries through the use of other spatial high order discretizations as the Chebyshev methods retaining the same characteristic of stability and efficiency. The type of discretizations presented here also offer great promise for the computation of complex fluid systems such as polymeric flows.

Acknowledgments

We thank P. Dimotakis, G. Fredrickson, C. Garcia-Cervera, D. Jacqmin, J. Langer, G. Leal, J. Lowengrub, E. Meiburg, and T. Y. Hou for helpful discussions. This work was partially supported by the National Aeronautics and Space Administration - Microgravity Research Division under the Contract No. NAG3-2414. H.D.C. acknowledges partial support from the Academic Senate Junior Faculty Research Award.

Appendix

Finite difference compact schemes

To achieve a uniform spectral-like accuracy we choose the finite difference compact schemes proposed by Lele [5]. These compact schemes have a "spectral like" wavenumber representation of the derivatives rather than having the lowest truncation error.

For the first derivative in the z (wall normal direction) we use the compact approximation scheme

$$\beta\hat{u}'_{i-2} + \alpha\hat{u}'_{i-1} + \hat{u}'_i + \alpha\hat{u}'_{i+1} + \beta\hat{u}'_{i+2} = c\frac{\hat{u}_{i+3} - \hat{u}_{i-3}}{6\Delta z} + b\frac{\hat{u}_{i+2} - \hat{u}_{i-2}}{4\Delta z} + a\frac{\hat{u}_{i+1} - \hat{u}_{i-1}}{2\Delta z}, \tag{44}$$

where the prime denotes derivative with respect z, and the caret stands for the 2D Fourier transform in the streamwise direction. The optimized coefficients for a "spectral-like" resolution are [5] $\alpha = 0.5771439$, $\beta = 0.0896406$, $a = 1.3025166$, $b = 0.99355$, $c = 0.03750245$.

At points neighboring boundaries $i = 3$ and $i = N_z - 2$, where N_z is the number of z grid points, we use an eight-order compact stencil in which $\alpha = \frac{4}{9}$, $\beta = \frac{1}{36}$, $a = \frac{40}{27}$, $b = \frac{25}{54}$, $c = 0$. For the points $i = 2$ and $i = N_z - 1$ we use a fourth order scheme with $\alpha = \frac{1}{4}$, $\beta = 0$, $a = \frac{10}{12}$, $b = 0$, $c = 0$.

The compact approximation schemes for the boundaries $i = 1$ and N_z are

$$\hat{u}'_1 + 2\hat{u}'_2 = \frac{1}{\Delta z}\left(-\frac{5}{2}\hat{u}_1 + 2\hat{u}_2 + \frac{1}{2}\hat{u}_3\right), \tag{45}$$

$$\hat{u}'_{N_z} + 2\hat{u}'_{N_z-1} = \frac{1}{\Delta z}\left(\frac{5}{2}\hat{u}_{N_z} - 2\hat{u}_{N_z-1} - \frac{1}{2}\hat{u}_{N_z-2}\right). \tag{46}$$

These are third order schemes [5,18].

To approximate the second derivative we use

$$\beta\ \hat{u}''_{i-2} + \alpha\hat{u}''_{i-1} + \hat{u}''_i + \alpha\hat{u}''_{i+1} + \beta\hat{u}''_{i+2} = \\ c\frac{\hat{u}_{i+3} - 2\hat{u}_i + \hat{u}_{i-3}}{9\left(\Delta z\right)^2} + b\frac{\hat{u}_{i+2} - 2\hat{u}_i + \hat{u}_{i-2}}{4\left(\Delta z\right)^2} + a\frac{\hat{u}_{i+1} - 2\hat{u}_i + \hat{u}_{i-1}}{\left(\Delta z\right)^2} \tag{47}$$

and the optimized coefficients for "spectral-like" resolution are $\alpha = 0.50209266$, $\beta = 0.05569169$, $a = 0.21564935$, $b = 1.723322$, and $c = 0.1765973$. At points neighboring boundaries $i = 3$ and $i = N_z - 2$ we use an eight-order compact stencil in which $\alpha = \frac{344}{1179}$, $\beta = \frac{23}{2358}$, $a = \frac{320}{393}$, $b = \frac{310}{393}$, $c = 0$ while for the points $i = 2$ and $i = N_z - 1$ we use a fourth order scheme with $\alpha = \frac{1}{10}$, $\beta = 0$, $a = \frac{6}{5}$, $b = 0$, $c = 0$. For the boundaries we choose

$$\hat{u}''_1 + 11\hat{u}''_2 = \frac{1}{\left(\Delta z\right)^2}\left(13\hat{u}_1 - 27\hat{u}_2 + 15\hat{u}_3 - \hat{u}_4\right), \tag{48}$$

$$\hat{u}''_{N_z} + 11\hat{u}''_{N_z-1} = \frac{1}{\left(\Delta z\right)^2}\left(13\hat{u}_{N_z} - 27\hat{u}_{N_z-1} + 15\hat{u}_{N_z-2} - \hat{u}_{N_z-3}\right). \tag{49}$$

These are third order accurate schemes with a truncation error ten times smaller than that of the analogous explicit one (see [5,18]).

Properties of Sine and Cosine Transforms

We define the Fourier cosine and sine transforms of a function $f\left(x\right)$ as

$$C\left[f\left(x\right)\right] = \frac{2}{\pi}\int_0^\infty f\left(x\right)\cos\omega x dx \tag{50}$$

$$S\left[f\left(x\right)\right] = \frac{2}{\pi}\int_0^\infty f\left(x\right)\sin\omega x dx \tag{51}$$

Integration by parts can be used to obtain this formula for the transforms of first derivative

$$S\left[\frac{df}{dx}\right] = -\omega C[f] \tag{52}$$

under the hypothesis of compact support for $f\left(x\right)$. We used this transformation to calculate the z-derivatives in the real space of $\nabla\phi$ and ∇p.

For the second derivatives we have,

$$C\left[\frac{d^2f}{dx^2}\right] = -\frac{2}{\pi}\frac{df}{dx}(0) - \omega^2 C[f] \tag{53}$$

under the hypothesis of compact support for $f(x)$ and $f'(x)$.

For the fourth derivative we have,

$$C\left[\frac{d^4f}{dx^4}\right] = -\frac{2}{\pi}\left(\frac{d^3f}{dx^3}(0) - \omega^2\frac{df}{dx}(0)\right) + \omega^4 C[f] \tag{54}$$

under the hypothesis of compact support for $f(x)$, $f'(x)$ and $f'''(x)$. We used these properties to solve the Cahn-Hilliard and the Poisson equations; for the Cahn-Hilliard equation $f'(0) = f'''(0) = 0$ thanks to the boundary conditions (4) and for the Poisson equation $f'(0) = 0$ thanks to the boundary condition (24). Note that these properties hold for the discrete transforms as well.

References

[1] J. W. Cahn, J. E. Hilliard, Free energy of a nonuniform system I, J. Chem. Phys. 28 (1958) 258.

[2] J. W. Cahn, J. E. Hilliard, Free energy of a nonuniform system III, J. Chem. Phys. 31 (1959) 688.

[3] P. C. Hohenberg, B. I. Halperin, Theory of dynamic critical phenomena, Rev. Mod. Phys. 49 (3) (1977) 435.

[4] J. Lowengrub, L. Truskinovsky, Quasi-incompressible Cahn-Hilliard fluids and topological transitions, Proc. R. Soc. London A 454 (1998) 2617.

[5] S. K. Lele, Compact finite difference schemes with spectral-like resolution, J. Comput. Phys. 103 (1992) 16.

[6] R. Chella, V. Viñals, Mixing of a two-phase fluid by a cavity flow, Phys. Rev. E 53 (1996) 3832.

[7] D. Jacqmin, Calculation of two phase Navier Stokes flows using phase-field modeling, J. Comput. Phys. 115 (1999) 96.

[8] V. M. Kendon, M. E. Cates, I. P. Barraga, J.-C. Desplat, P. Blandon, Inertial effects in three-dimensional spinodal decomposition of a symmetric binary fluid mixture: a lattice Boltzmann study, J. Fluid Mech. 440 (2001) 147.

[9] Y. Wu, H. Skrdla, T. Lookman, S. Chen, Spinodal decomposition in binary fluids under shear flow, Physica A 239 (1997) 428–436.

[10] O. Penrose, P. Fife, Thermodynamically consistent models of phase-field type for the kinetics of phase transitions, Physica D 43 (1990) 44.

[11] P. W. Bates, P. C. Fife, The dynamics of nucleation for the Cahn-Hilliard equation, SIAM J. Appl. Math. 53 (1993) 990.

[12] C. M. Elliot, The Cahn-Hilliard model for the kinetics of phase separation, in: J. F. Rodrigues (Ed.), Mathematical Models for Phase Change Problems, Vol. 88 of International Series of Numerical Mathematics, Bikhäuser Verlag Basel, 1989, pp. 35–72.

[13] M. E. Gurtin, D. Polignone, J. Viñals, Two-phase binary fluids and immiscible fluids described by an order parameter, Math. Models Meth. Appl. Sci. 6 (6) (1996) 815.

[14] A. J. Bray, Theory of phase-ordering kinetics, Advances in Physics 43 (3) (1994) 357–459.

[15] J. D. van der Waals, The thermodynamic theory of capillarity flow under the hypothesis of a continuous variation of density (in dutch), Verhandel/Konink. Akad. Weten. 1 (1879) 8.

[16] J. S. Langer, M. Baron, H. Miller, New computational method in theory of spinodal decomposition, Phys. Rev. A 11 (4) (1975) 1417.

[17] A. W. Cook, P. E. Dimotakis, Transition stages of Rayleigh-Taylor instability between miscible fluids, J. Fluid. Mech. 443 (2001) 69.

[18] J. C. Buell, A hybrid numerical-method for 3-dimensional spatially-developing free shear flows, J. Comput. Phys. 95 (2) (1991) 313–338.

[19] J. J. Douglas, T. Dupont, Alternating-direction galerkin methods on rectangles, in: B. Hubbard (Ed.), SYNSPADE-1970, Numerical Solution of Partial Differential Equations-II, Academic Press, New York, 1971, pp. 133–213.

[20] D. Gottlieb, S. A. Orszag, Numerical Analysis of Spectral Methods: Theory and Applications, CBMSNSF Regional conference series in applied mathematics, SIAM Press, 1977.

[21] H. D. Ceniceros, A semi-implicit moving mesh method for the focusing Schrödinger equation, Commun. Pure Appl. Anal. 1 (2002) 1.

[22] D. J. Eyre, An unconditionally stable one-step scheme for gradient systems, preprint.

[23] J. Zhu, L.-Q. Chen, J. Shen, V. Tikare, Coarsening kinetics from a variable-mobility Cahn-Hilliard equation: Application of a semi-implicit Fourier spectral method, Phys. Rev. E 60 (4) (1999) 3564–3572.

[24] A. J. Chorin, Numerical solution of the Navier-Stokes equations, Math. Comp. 22 (1968) 745.

[25] R. Temam, Sur l'approximation de la solution des equations de Navier-Stokes par la méthode des pas fractionnaires (II), Arch. Rational Mech. Anal. 33 (5) (1969) 377.

[26] R. Temam, Remark on the pressure boundary condition for the projection method, Theoret. Comput. Fluid Dynamics 3 (1991) 181.

[27] S. A. Orszag, M. Israeli, M. O. Deville, Boundary conditions for incompressible flows, J. Sci. Comput. 1 (1986) 75.

[28] W. E, J.-G. Liu, Projection method I: convergence and numerical boundary layers, SIAM J. Numer. Anal. 32 (4) (1995) 1017.

[29] M. Kang, R. Fedkiw, X.-D. Liu, A boundary condition capturing method for multiphase incompressible flow, J. Sci. Computing 15 (2000) 323–360.

[30] C. W. Shu, S. Osher, Efficient implementation of essentially non-oscillatory shock capturing schemes, J. Comput. Phys. 88 (1988) 439.

[31] M. Sussman, P. Smereka, S. Osher, A level set approach for computing solutions to incompressible two-phase flow, J. Comput. Phys. 114 (1994) 146–159.

[32] J. U. Brackbill, D. B. Kothe, C. Zemach, A continuum method for modeling surface tension, J. Comput. Physics 100 (1992) 335.

[33] G. I. Taylor, The formation of emulsions in definable fields of flows, Proc. R. Soc. Lond. A146 (1934) 501–523.

[34] M. Shapira, S. Haber, Low reynolds number motion of a droplet in shear flow including wall effects, Int. J. Multiphase Flow 16 (2) (1990) 305–321.

[35] J. M. Rallison, The deformation of small viscous drops and bubbles in shear flow, Ann. Rev. Fluid Mech. 16 (1984) 45–66.

[36] M. Copetti, C. Elliot, Kinetics of phase decomposition process: numerical solutions to the Cahn-Hilliard equation, Material Sci. Technol. 6 (1990) 273.

[37] A. Chakrabarti, R. Toral, J. D. Gunton, Late-stage coarsening for off-critical quenches: Scaling functions and the growth law, Phys. Rev. E 47 (1993) 3025–3038.

[38] A. Onuki, Phase transitions of fluids in shear flow, J. Phys.: Cond. Matter 9 (1997) 6119.

[39] A. Frischknecht, Stability of cylindrical domains in phase-separating binary fluids in shear flow, Phys. Rev. E 58 (3) (1998) 3495–3514.

[40] T. Hashimoto, K. Matsuzaka, E. Moses, A. Onuki, String phase in phase-separating fluids under shear flow, Phys. Rev. Lett. 74 (1) (1995) 126–129.

[41] K. B. Migler, String formation in sheared polymer blends: coalescence, breakup, and finite size effects, Phys. Rev. Lett. 86 (6) (2001) 1023–1026.

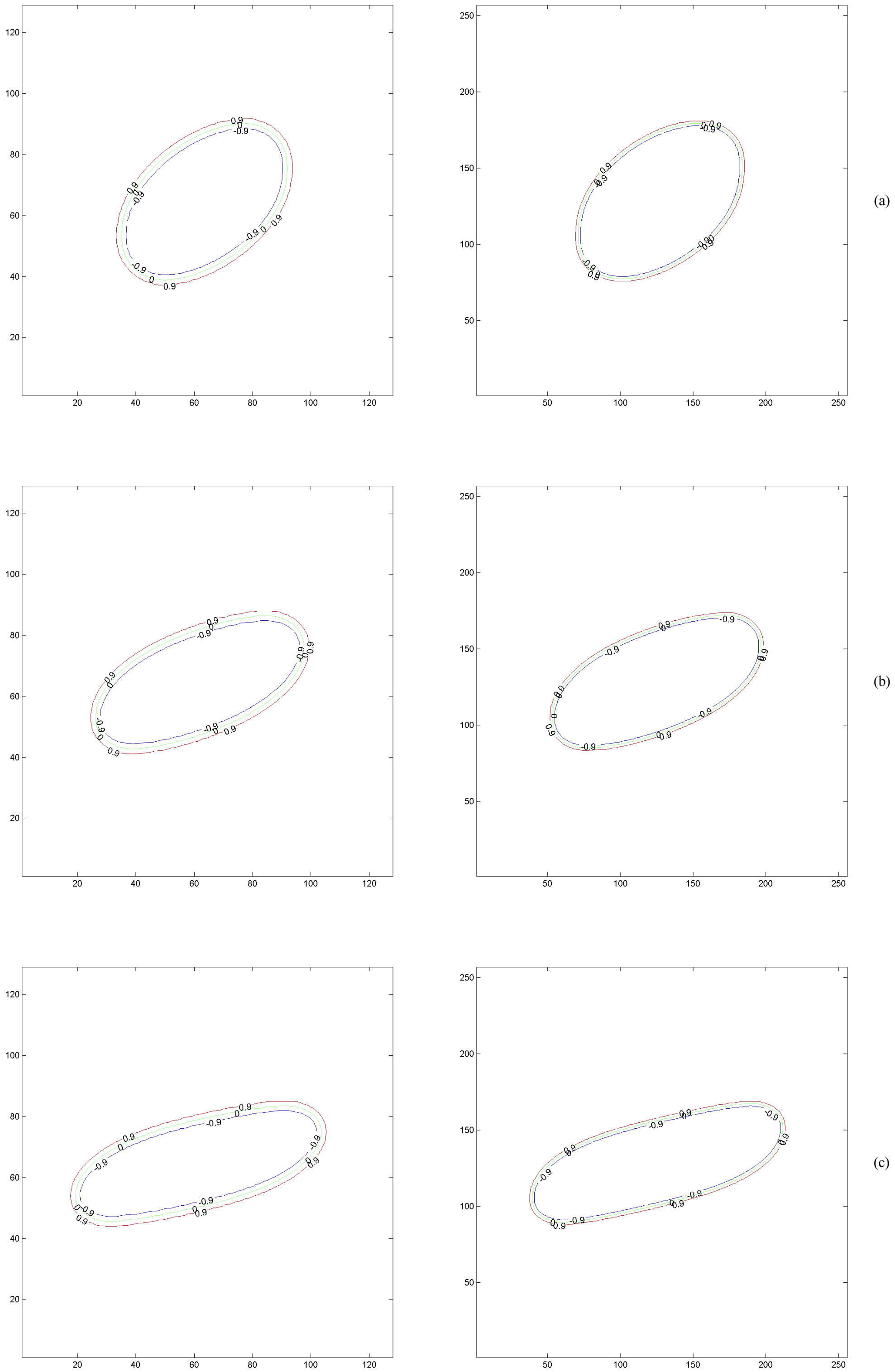

Fig. 1. 2D deformation of an initially spherical drop described by ϕ, $Pe = 10$, $Re = 0.1$,for (a) $Ca = 0.6$,, (b) $Ca = 0.9$, and (c) $Ca = 1.2$. First column $N = 128$ and $L = 178$, second column $N = 256$ and $L = 355$.

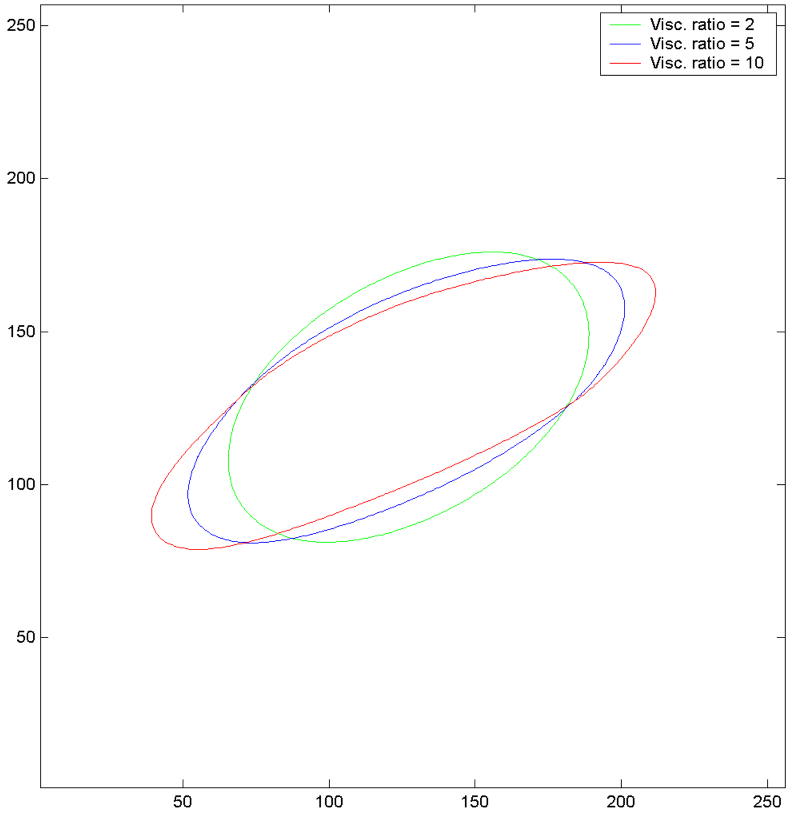

Fig. 2. 2D deformation of an initially spherical drop described by ϕ, $Pe = 10$, $Re = 0.1$, $Ca = 0.8$, $\theta_{\max} = 2$, 5 and 10, $N = 256$ and $L = 355$.

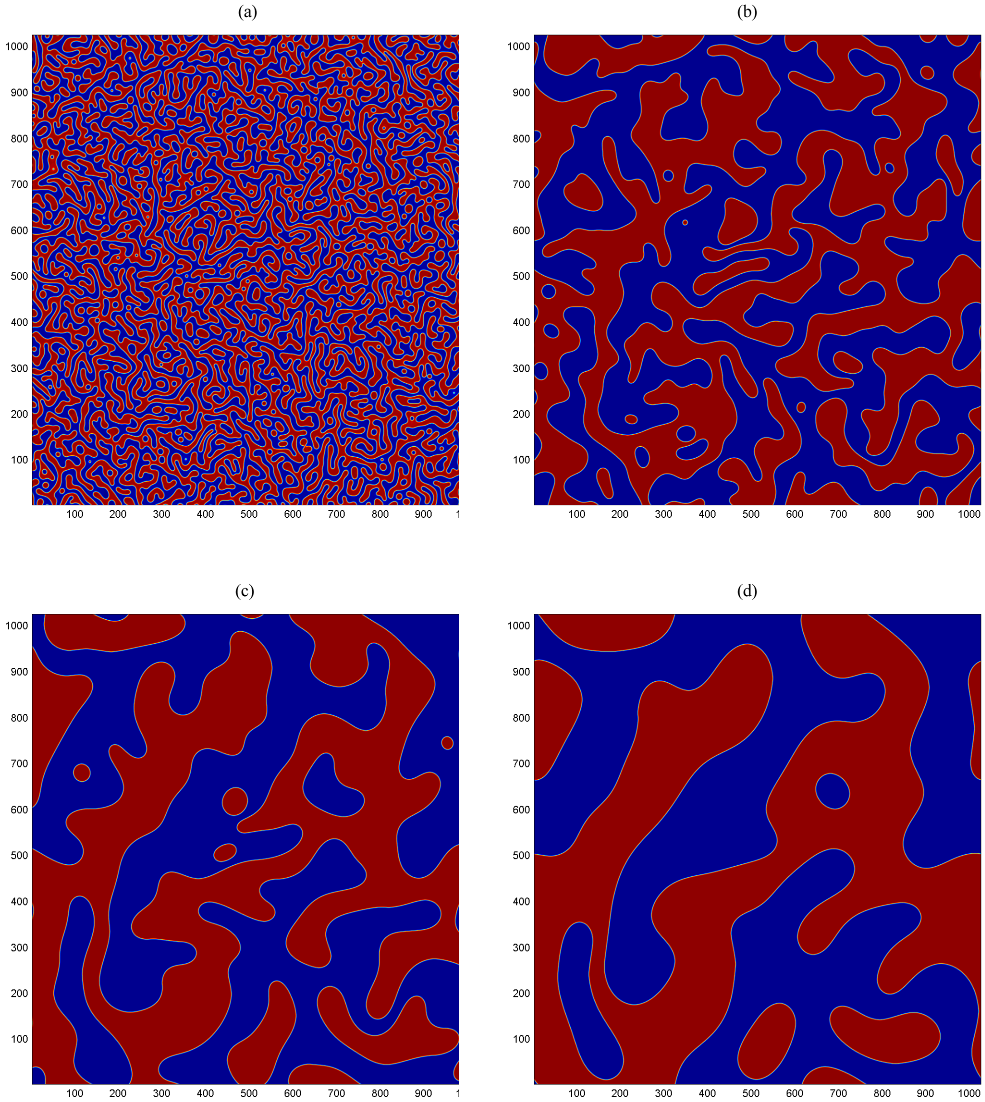

Fig. 3. Evolution of ϕ, represented in flooded contours, at different times. (a) $t = 6.93 \times 10^{-4}$, (b) $t = 0.36$, (c) $t = 1.16$, (d) $t = 2.76$. $N = 1024$, $\gamma = 0$, $\phi_m = 0$, $C = 7.03 \times 10^{-4}$ and $\Delta t = 4.95 \times 10^{-7}$ for (a), $\Delta t = 0.0002$ for (b)-(d)

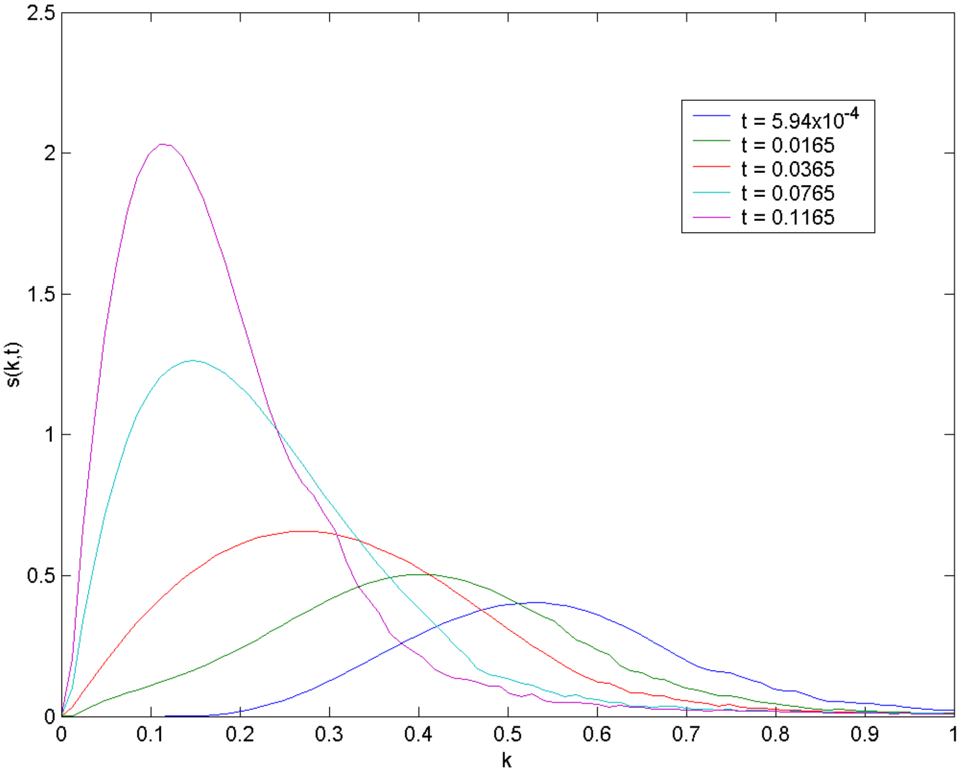

Fig. 4. Structure function as a function of k at five different time steps for bulk-diffusion-controlled coarsening.

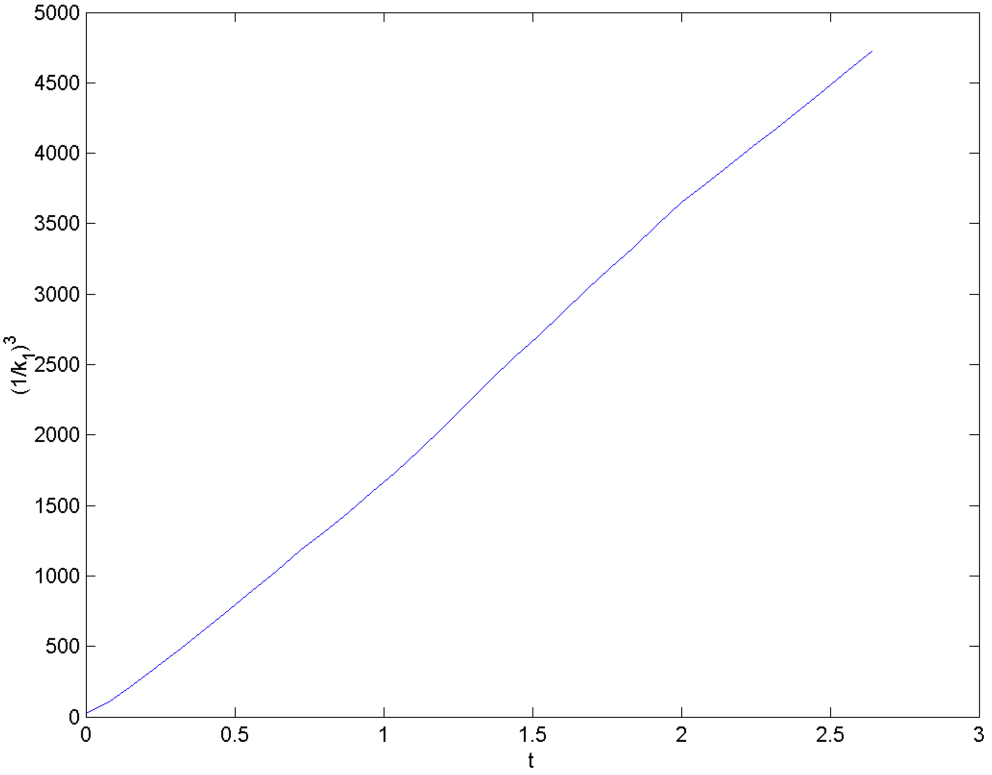

Fig. 5. The cubic of the average domain size vs time at the late stage of bulk-diffusion-controlled coarsening (domain size characterized by $(1/k_1)$)

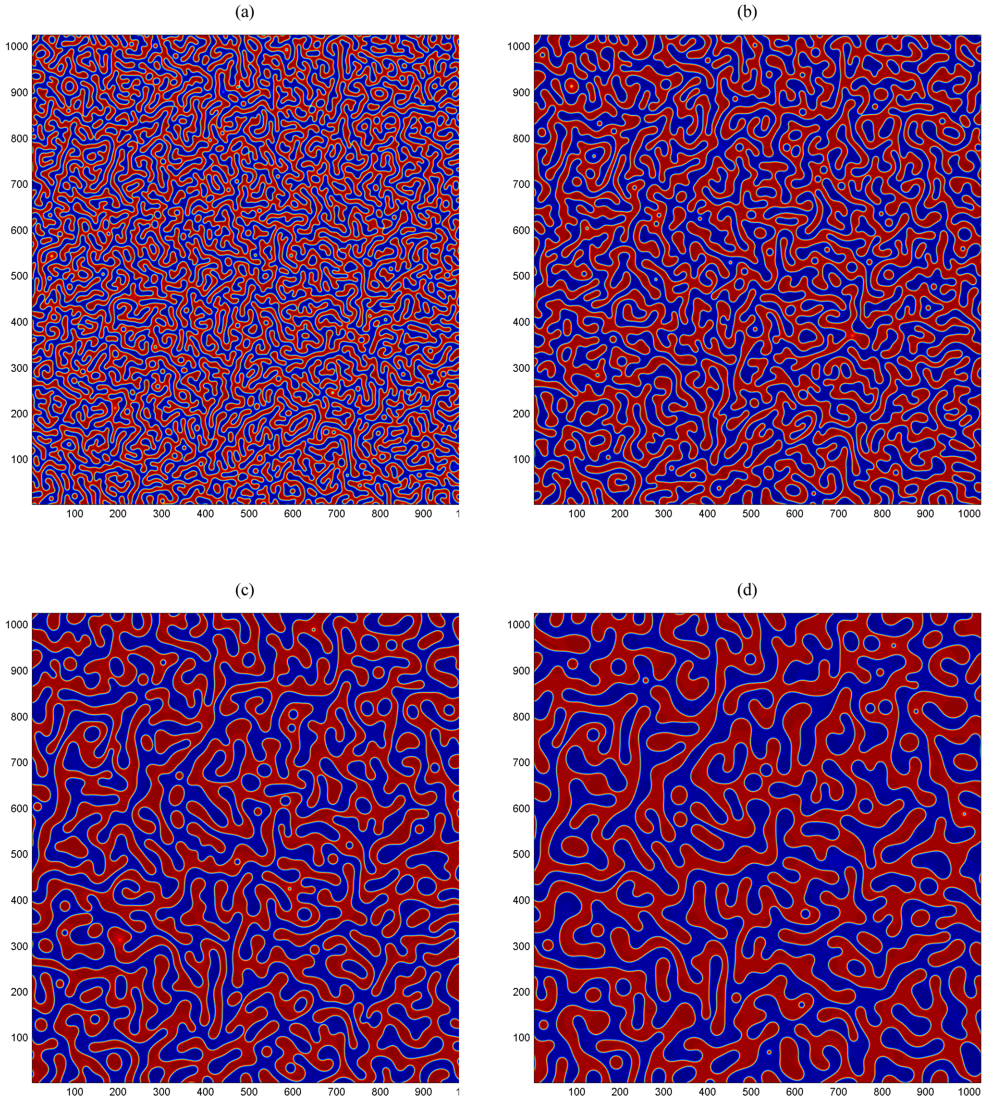

Fig. 6. Variable mobility: evolution of ϕ, represented in flooded contours, at different times. (a) $t = 0.1$, (b) $t = 0.47$, (c) $t = 1.4$, (d) $t = 3.0$. $N = 1024$, $\gamma = 0.9$, $\phi_m = 0.0$, $C = 0.001$ and $\Delta t = 0.01$ for (a)-(d).

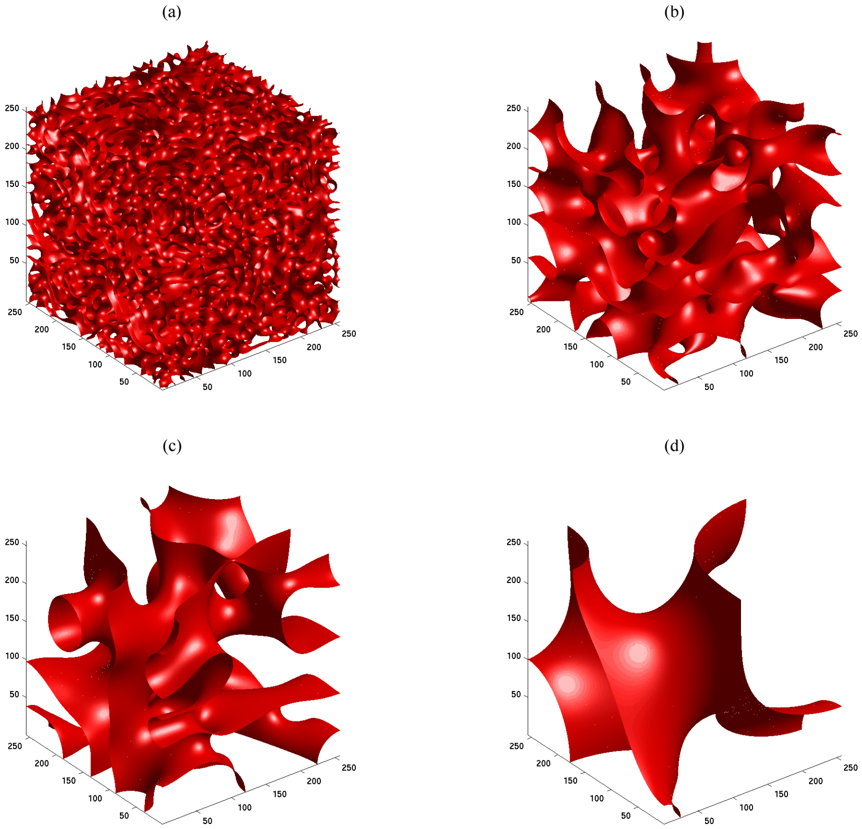

Fig. 7. Evolution of ϕ represented by the iso-surfaces of separation of the two fluids at $\phi = 0.0$, at different times. (a) $t = 0.0375$, (b) $t = 6.5$, (c) $t = 14.0$, (d) $t = 94.0$. $N = 256$, $\gamma = 0.0$, $\phi_m = 0.0$ and $\Delta t = 2.5 \times 10^{-4}$ for (a), $\Delta t = 0.01$ for (b), (c) and (d).

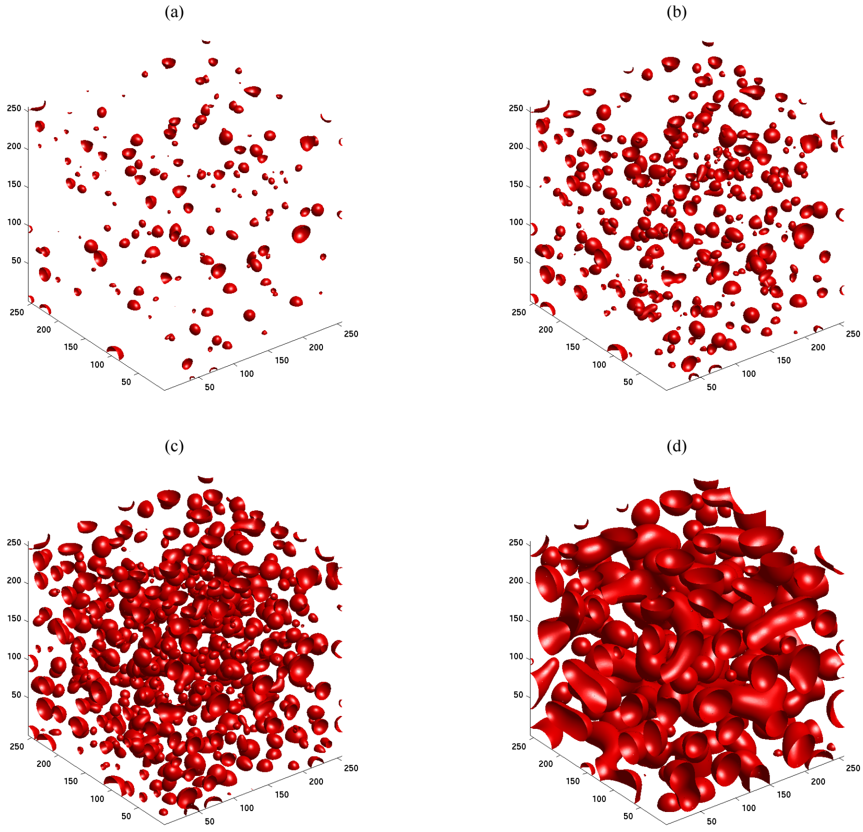

Fig. 8. Evolution of ϕ represented by the iso-surfaces of separation of the two fluids at $\phi = 0.0$, at different times. (a) $t = 0.10375$, (b) $t = 0.10475$, (c) $t = 0.10625$, (d) $t = 0.15$. $N = 256$, $\gamma = 0.0$, $\phi_m = -0.5$ and $\Delta t = 2.5 \times 10^{-4}$ for (a), (b), (c) and (d).

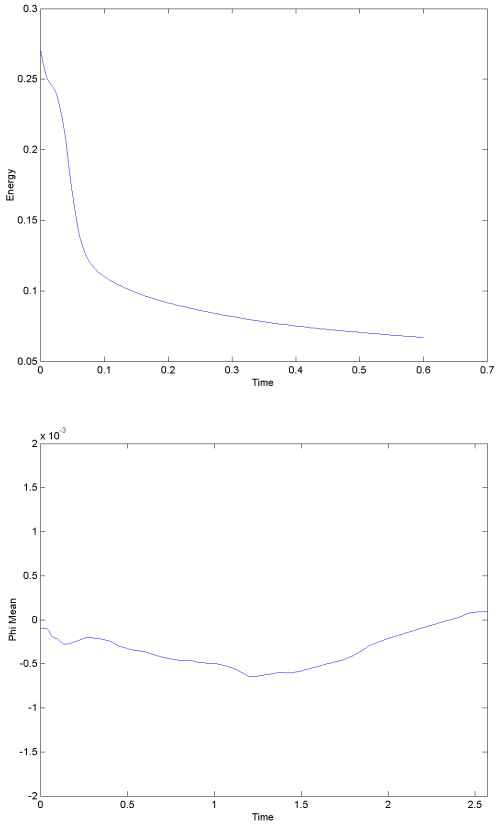

Fig. 9. Behavior of the mean ϕ_m and of the energy $F(\phi)$ in time for the semi-implicit scheme for $\phi_m(t=0)=0$.

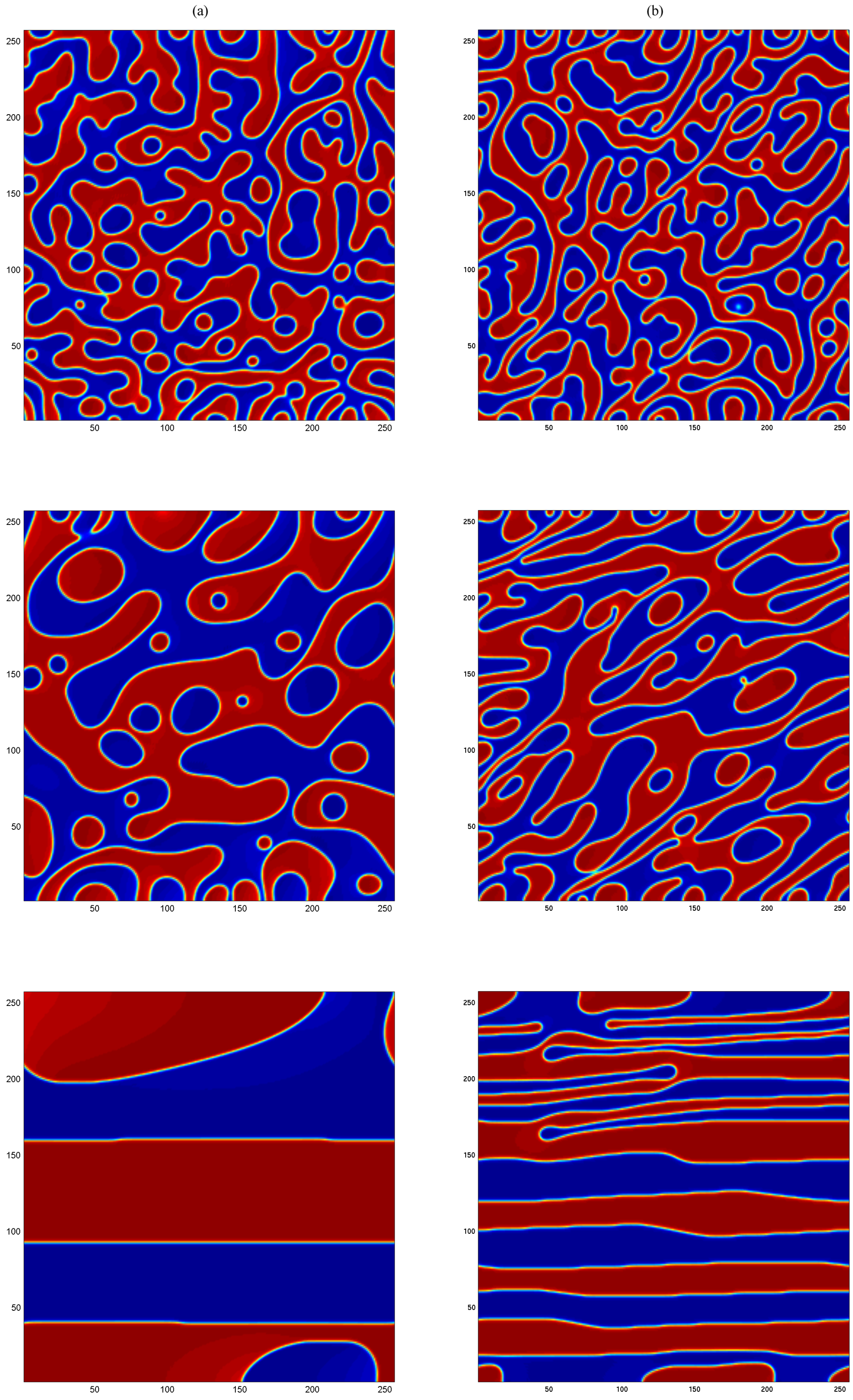

Fig. 10. 2D spinodal decomposition in a channel under shear, (a)(First Column) $Pe = 7.5$, $Re = 0.1$, and $Ca = 0.5$, (b) (Second column) $Pe = 37.5$, $Re = 0.5$, and $Ca = 2.5$. $N = 256$ and $L = 355$.

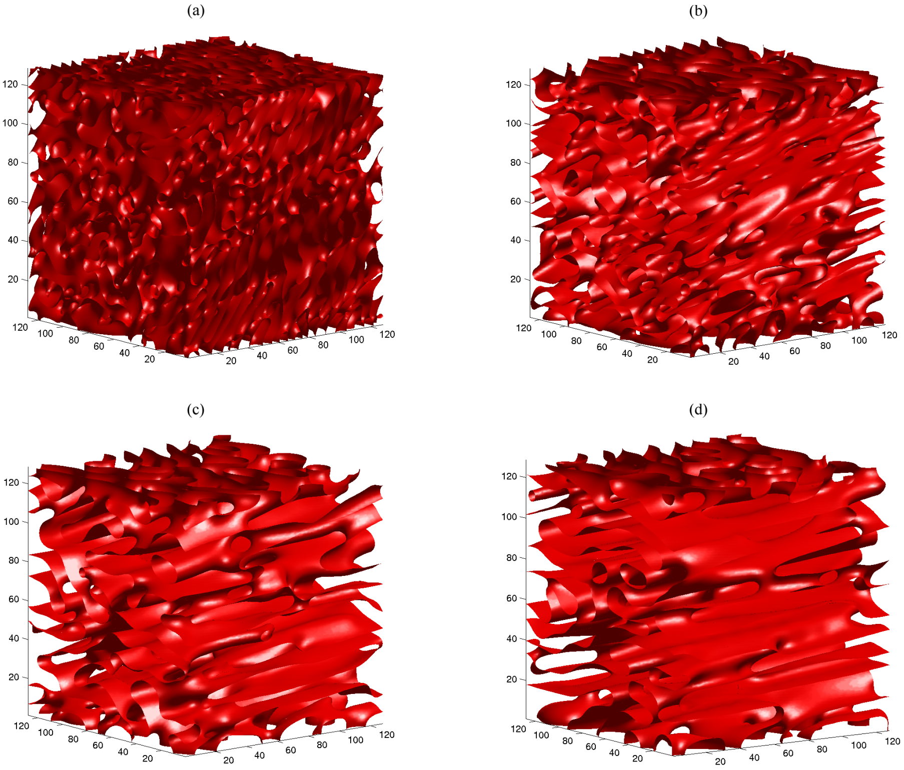

Fig. 11. 3D spinodal decomposition in a channel under shear, $Pe = 5$, $Re = 0.12$, $Ca = 20$, $N = 128$ and $L = 178$. (a) $t = 1080$, (b) $t = 3600$, (c) $t = 7200$, (d) $t = 9000$.